PSF calibration using the Lyot-based low order wavefront sensor telemetry: First simulations

Garima Singh[a], Julien Lozi[b], Elodie Choquet[a*], Eugene Serabyn[a] and Olivier Guyon[b]

[a]Jet Propulsion Laboratory, California Institute of Technology, 4800 Oak Grove Drive, Pasadena, CA 91109-8099, USA;
[b]National Astronomical Observatory of Japan, Subaru Telescope, 650 N A'Ohoku Place, Hilo, HI 96720, USA

ABSTRACT

One of the factor that derives the performance of small inner working angle (IWA) coronagraphs is the quality of the low-order wavefront calibration and control. The uncorrected residuals scatter the starlight and produces intensity fluctuations, which as a result creates dynamic speckle noise in the focal plane. To improve post processing of the science images, the low-order telemetry of the residuals left uncorrected by the control loop can be used to calibrate the amount of starlight leakage at small angular separations. In this proceeding, we present the preliminary simulations of point spread function calibration using the Lyot-based low-order wavefront sensor measurements (tip-tilt only) for a vector vortex coronagraph.

Keywords: High contrast Imaging, Low-order wavefront aberrations, Extreme adaptive optics systems, Coronagraphy

1. INTRODUCTION

High performance small IWA coronagraphs equipped with ground-based extreme adaptive optics (ExAOs) systems can image exoplanets in the inner regions (< 10 AU) of the extrasolar systems.[1] Gaining access to immediate neighborhood of a star is crucial as it allows to search exoplanets in the possible habitable zone. Apart from improving coronagraphs design, an important factor that rule system performance is the nature of wavefront control.[2] Small IWA coronagraphs are highly sensitive to the low-order wavefront aberrations.[1] Uncorrected residuals lead to starlight leak around the edge of a focal plane mask (FPM), which contributes to speckle noise in the science image at small IWA. Possible signal from a faint companion can easily be overwhelmed by this uncontrolled speckle noise.[3]

Sensors such as the coronagraphic low-order wavefront sensor (CLOWFS[4]), the Lyot-based low-order wavefront sensor (LLOWFS[5]) and the Zernike wavefront sensor[6] exist providing measurement and correction of the low-order wavefront errors. In addition, the knowledge of wavefront sensor (WFS) telemetry, can address the residual speckle noise left uncorrected by the non common path aberrations (NCPA) and also the time lag between the low-order errors measurement and correction. Although, techniques like angular differential imaging[7] can calibrate out the static and quasi-static speckle features but becomes less effective at angular separation smaller than 0.5 arcseconds[8] because of signal self-subtraction. One previously discussed solution[9] is to use the WFS telemetry saved during the science observation to subtract the point spread function (PSF) artifacts contributed by the residuals left uncorrected by the WFS. Following this idea, we performed simulation using the LLOWFS, which was developed to address low-order aberrations in small IWA phase mask coronagraphs. LLOWFS, using the starlight reflected by the Lyot stop, reliably measures[10,11] up to 35 low-order Zernike modes and is fully operational on the Subaru Coronagraphic Extreme Adaptive Optics (SCExAO[12]) instrument at the Subaru Telescope.

Prior of on-sky science acquisition, the PSF can be calibrated by recording synchronized low-order measurements using LLOWFS and science camera images. These frames are used to build a library of response of the

* Hubble Fellow
Send correspondence to the author: garima.singh@jpl.nasa.gov

residuals on the starlight leakage. During the observation of the science target, LLOWFS residuals can be fitted with the best match in the library. The corresponding science equivalents can then either be subtracted from the science image or can be inputted to the Principal Component Analysis (PCA[13]) algorithm as reference images to reconstruct the PSF. This technique can significantly improve the sensitivity of a coronagraph.

The first part of the article describes the principle and working of LLOWFS. In §2, a detailed concept of LLOWFS (§2.1) and a procedure of measuring and correcting (§2.2) the low-order aberrations are described. §2.5 briefly introduce LLOWFS results on the SCExAO instrument. In the second part of the article (§3), we describe simulations of PSF reconstruction and subtraction using the LLOWFS telemetry.

2. LYOT-BASED LOW-ORDER WAVEFRONT SENSOR

2.1 LLOWFS Theory

Specifically designed for the small IWA coronagraphs,[11] LLOWFS is a new generation of coronagraphic wavefront sensor which reimages the residual starlight reflected by the Lyot stop. Using a single defocused image, LLOWFS efficiently measures the low-order wavefront aberrations. Based on the coronagraphic theory, we will first briefly explain the general formalism of imaging through a LLOWFS system. Figure 1 represents the optical layout of a LLOWFS imaging system. Following the Fraunhofer approximation in which the complex amplitude at the focal plane is the Fourier transform of the electric field (EF) at the pupil plane, we can collectively write the EF $\psi_E(\xi, \lambda)$ inside the Lyot plane in the shown coronagraphic system as follows

$$\frac{\psi_E(\xi, \lambda)}{\psi_0} = (P * \mathcal{F}^{-1}[M])L + i\ (\phi * \mathcal{F}^{-1}[M])L\ , \tag{1}$$

where $\mathcal{F}$ denotes the Fourier transform; P is the entrance pupil; ψ_0 represents the on-axis star flux upstream of the coronagraph; λ is the wavelength at which the star is observed; ξ is the coordinate inside the pupil plane at an instant t; ϕ is the phase aberration induced at the position ξ in P; M is a focal plane mask (FPM), which is optically conjugated to the final detector plane and filters out the starlight at low spatial frequency; and L is a diaphragm called the Reflective Lyot Stop (RLS), which is optically conjugated with P and is used to reimage the filtered out diffracted starlight from outside the edge of the geometrical pupil. The complex amplitude $A_E(x)$ of the field at the Lyot plane can be written as $\mathcal{F}[\psi_E]$, where x is the 2-D coordinate in the image plane.

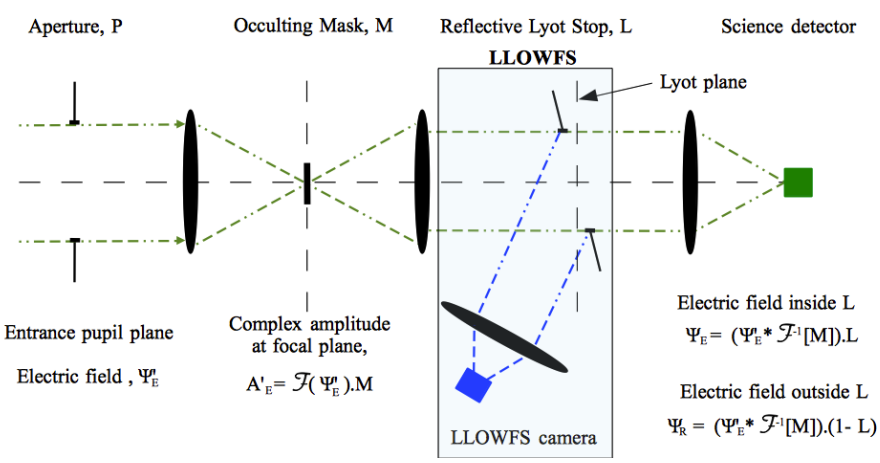

Figure 1. General formalism of imaging through a LLOWFS system. Fourier transformation ($\mathcal{F}$) is used to study the complex amplitude of the field at different focal and pupil planes.

In Fig. 1, if we look outside of the geometrical pupil at the Lyot plane, the EF $\psi_R(\xi, \lambda)$ can be written as

$$\frac{\psi_R(\xi, \lambda)}{\psi_0} = (P * \mathcal{F}^{-1}[M])(1 - L) + i\ (\phi * \mathcal{F}^{-1}[M])(1 - L)\ . \tag{2}$$

$\psi_R(\xi,\lambda)$ represents the complex field reflected downstream of RLS in the highlighted LLOWFS channel. Now expanding the Eq. 2

$$\frac{\psi_R(\xi,\lambda)}{\psi_0} = (P * \mathcal{F}^{-1}[M]) - (P * \mathcal{F}^{-1}[M])L + i\ (\phi * \mathcal{F}^{-1}[M])(1-L)\ . \tag{3}$$

Consider a perfect coronagraph without any manufacturing defects. For a perfectly aligned on-axis star at the center of the FPM (M), the residual diffracted starlight downstream the FPM is rejected completely outside of the geometrical pupil and the electric field ($\psi_E(\xi,\lambda)$) is zero inside the Lyot pupil plane. One can then analytically equate the complex amplitude of $(P * \mathcal{F}^{-1}[M])L$ in Eq. 3 to 0.

The term $(P * \mathcal{F}^{-1}[M])$, is independent of ϕ which dictates that even when the wavefront is perfect, there is already some light at the LLOWFS focal plane (at the LLOWFS camera in Fig. 1). The complex amplitude A_R at LLOWFS focal plane is then obtained by taking the Fourier transform of the complex electric field $\psi_R(\xi,\lambda)$ outside the Lyot pupil plane. A_R is then written as

$$\frac{A_R(x)}{\psi_0} = (\mathcal{F}[P]M) + i\ (\mathcal{F}[\phi]M) * \mathcal{F}[(1-L)]\ . \tag{4}$$

Replacing the term $(\mathcal{F}[P]M)$ by A_0 and $i\ (\mathcal{F}[\phi]M) * \mathcal{F}[(1-L)]$ by $G[\phi]$, Eq. 4 becomes

$$\frac{A_R(x)}{\psi_0} = A_0 + G[\phi]\ , \tag{5}$$

where A_0 the complex amplitude obtained by the LLOWFS camera for a perfect wavefront.

By definition, any optical system is linear in complex amplitude. So the complex amplitude A_R obtained in LLOWFS camera is a linear function of the pupil plane complex amplitude A_E. The aberration-free complex amplitude distribution A_R in the LLOWFS camera and the change introduced on this complex amplitude by the low-order modes to be measured is nonorthogonal.

Since Eq. 5 is a linear function of ϕ in complex amplitude

$$\frac{A_R(x)}{\psi_0} = A_0 + mG[\phi]\ , \tag{6}$$

where m is a linear operator. The corresponding reflected light intensity $I_R = |A_R|^2$ in the LLOWFS camera is

$$I_R = I_0 + 2Re[A_0\overline{mG[\phi]}] + |mG[\phi]|^2\ , \tag{7}$$

where I_0 corresponds to the reflected intensity with no wavefront aberration. We will call I_0 as a reflected reference image throughout the article. I_R is then a linear function of $G[\phi]$ as long as

$$|mG[\phi]|^2 \ \ll\ Re[A_0\overline{mG[\phi]}]\ . \tag{8}$$

Equation 8 is satisfied if and only if $|mG[\phi]| \ll |A_0|$, which holds true only for small wavefront aberrations. Thus we define the basis of LLOWFS theory as

$$I_R = I_0 + 2Re[A_0\overline{mG[\phi]}]\ . \tag{9}$$

2.2 Measurement and correction of the low-order modes

At the entrance pupil of Fig. 1, lets consider that the wavefront is composed of low-order modes i of amplitude $\boldsymbol{\alpha} = (\alpha_1, \alpha_2 \cdots \alpha_n)$, where n is the total number of modes. For small aberrations, $\phi \ll 1$ radian root mean square (RMS) (which is a typical value of a post-AO wavefront residuals), any reference subtracted LLOWFS image (I_R) can be projected on to the basis of low-order modes i.e can be decomposed linearly on a base of orthonormal images S_i corresponding to the response of the sensor to the low-order modes. A general mathematical equation following this formalism is defined as follows

$$I_{R(\alpha)} - I_0 = \sum_{i=1}^{n} \alpha_i S_i + \nu_n \ , \tag{10}$$

where ν_n is the residual coming from the modes higher than the n-th mode. However, this equation is valid only if the reference image I_0 stays constant for the duration of the experiment. As the measurements are relative to a zero-point, the reference should be stable in order for the linear model in Eq. 10 to remain consistent.

For the optimal performance of LLOWFS closed-loop operation, the measurements α_i of the low-order errors in Eq. 10 are done through the singular value decomposition method by pseudo-inverting the response matrix S (composed of the calibration frames S_i computed for each mode i) to provide the optimal solution to the least-squares problem in Eq. 10. Figure. 2 shows a schema of closed-loop control operation of the LLOWFS that follows a simple integrator control law to compute the correction phasemap. This correction is then subtracted from the current actuator phasemap of the actuator, for example a deformable mirror. The correction applied on the DM compensate for most of the low-order aberrations in image I_R.

2.3 Defocus in the sensor position

For centrosymmetric aberrations (focus and the spheric aberrations), LLOWFS camera can estimate their amplitudes but not their signs, because of their symmetry around the focal plane. As a result, these modes create an orthogonality between A_0 and $mG[\phi]$, which implies to $Re[A_0\overline{mG[\phi]}] = 0$, thus violating the Eq. 8. In that case, the LLOWFS image I_R in Eq. 7 becomes a quadratic function of the wavefront aberrations, $I_R = I_0 + |m\phi|^2$. This orthogonality is broken by introducing a defocus in the position of the LLOWFS camera. The value for the defocus should be chosen carefully, which can be different for different coronagraphs as it depends on how a FPM is redistributing the starlight and where most of the light is concentrated (for a Phase-Induced Amplitude Apodization [**?**, PIAA,]]piaa coronagraph, the reflected light is concentrated in an annulus whereas for a VVC, most of the light is at the center of the LLOWFS PSF) in the reimaged LLOWFS camera plane.

The defocus value is the tradeoff between the number of modes to be corrected and the speed of the sensor. A large defocus allows to correct more modes but spreads the signal over a larger number of pixels, which requires to integrate longer. A small defocus is more adapted for faint stars but does not allow to correct a lot of modes. Therefore, during on-sky closed-loop operations, the amount of sensor defocus should be selected depending on the detector and the brightness of the star. For our experiments, we choose 15 radian RMS of defocus as it produces clean modes and give relatively better performance in sensor measurements.

2.4 Calibration frames S_i

Real time control of the low-order aberrations by the LLOWFS requires a prior calibration of the system response to the low-order modes. This is achieved by applying a pure Zernike phasemap upstream of the FPM for the mode i with an amplitude a_{ci} and measuring the linear response of the sensor (S_i, for a low-order mode i) to the applied mode. To obtain S_i, only an actuating element is required to send controlled amount of aberration in the coronagraphic system. A general equation is defined as,

$$S_i = \frac{I_{Ri} - I_0}{a_{ci}} \ , \tag{11}$$

where I_{Ri} is the LLOWFS image recorded by the LLOWFS camera for the mode i and I_0 is the reference image. Equation 11 is used to compute the response S_i for any i^{th} mode. Using these responses, a LLOWFS image is decomposed in to a linear sum of aberrations in Eq. 10.

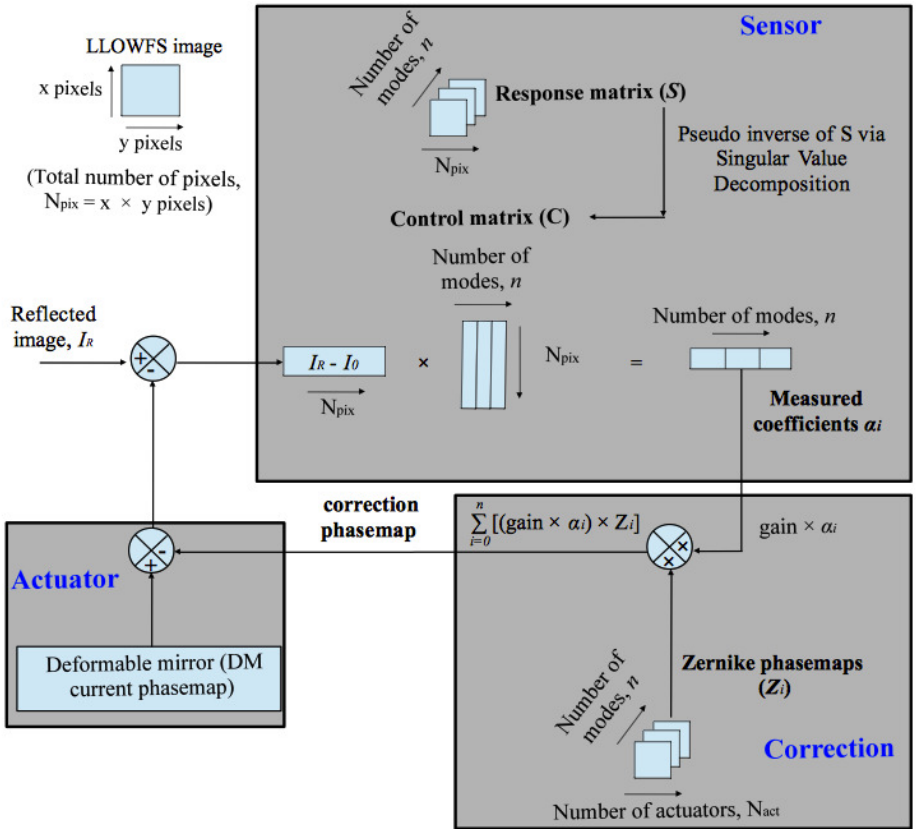

Figure 2. Control loop of the LLOWFS. In Eq. 10, the Pseudo inverse of the response matrix S through a singular value decomposition method returns the control matrix C, which in turn is used to get the measurements α_i of the unknown low-order errors. These measurements are used by an integrator controller to compute the correction, which are then sent to an actuating element such as a deformable mirror to compensate for the aberrations in the image I_R.

Stability of the reference image derives the requirement of reacquiring the calibration frames. Tip-tilt motions upstream of the FPM changes the shape of the LLOWFS PSF while downstream the FPM, NCPA change the position of the PSF on the LLOWFS camera. These NCPAs in the LLOWFS channel can be introduced only by the motion of the lens or the camera. During measurements of the low-order aberrations, the response of the sensor does not depend on the position of the PSF on the LLOWFS camera but does relies on its shape. However, while acquiring the calibration frames (the response S_i and the reference I_0), if any external factor such as temperature variations and the instrument flexure changes the position of the low-order PSF by introducing tip-tilt errors (positional errors) then a new calibration should be reacquired, prior of estimating the unknown low-order aberrations. Since these errors are not compensated, the tip-tilt upstream and downstream the FPM is assumed to remain stable during the acquisition of the calibration.

If these positional errors are out of the linear range and happen prior to closed-loop operation, then only the coronagraphic PSF need to be realigned behind the FPM and previously acquired calibration frames can be reused to close the loop. However such errors will not affect the closed-loop operation as the low-order correction will compensate for them.

2.5 LLOWFS on SCExAO

SCExAO instrument is Subaru Telescope's coronographic extreme adaptive optics instrument that uniquely combines four techniques – Extreme-AO: to measure high-order wavefront aberrations via a visible Pyramid wavefront sensor[14] with a frame rate of 3.6 kHz; Coronagraphy (IWA of 1-3 λ/D): to mask the on-axis starlight and suppress the diffraction effects of the telescope; LLOWFS: to keep the starlight centered on the FPM and

record residual wavefront errors for post-processing at 170 Hz and Speckle control: to modulate, suppress and calibrate residual speckles. SCExAO has its own 2000-actuator MEMS DM that provides actuation for all the wavefront sensing units as listed. AO188,[15] Subaru Telescope's adaptive optics system facility corrects 187 modes in the wavefront and feeds the residuals to SCExAO with a beam at $F/14$. The output from SCExAO can either go to its internal near-infrared (NIR) science camera or towards the HiCIAO science detector. Note that the operation of SCExAO is completely independent from the AO188.

LLOWFS efficiently stabilizes the starlight behind the FPM and routinely provides an on-sky pointing stability of 10^{-3} λ/D with its small IWA coronagraphs. Detailed on-sky operation of LLOWFS can be find in Ref. 11 (*PhD Thesis*).

3. PSF CALIBRATION USING LLOWFS TELEMETRY

The idea is not a novelty. Ref. 9 has used the telemetry of a coronagraphic low-order wavefront sensor (CLOWFS[4]) to improve the subtraction of coronagraphic leaks due to low-order aberrations in a long exposure image. Their procedure was composed of calibrating the variations in optical path by building a dictionary of CLOWFS and science images, tracking low-order aberrations during a long science exposure and then post processing the data by identifying a match for each CLOWFS image in the long exposure data with the one in the dictionary to calibrate the uncorrected pointing errors. The match was based on pixel to pixel deviation between the two images averaged over the region of interest.

In their laboratory setup on the SCExAO instrument, the vibrations (using an electric water pump) were introduced to acquire a 25 minute sequence of 15000 pairs of 1 millisecond exposure images with both the CLOWFS and the science camera simultaneously. From this dictionary, 150 adjacent pairs of CLOWFS and science images were isolated to simulate a long-exposure acquisition. The short exposure science camera images are then selected from the dictionary that best match the residuals attributed to varying low-order aberrations in the long exposure coronagraphic image. Finally, the co-add of selected images from the dictionary is subtracted from the long exposure to calibrate the pointing residuals.

A 40 times improvement of the detection limit has been demonstrated at 4.75 λ/D for a Lyot coronagraph over a classical calibration procedure. However, the technique is not effective during on-sky operations as the dictionary focuses on calibrating only the static optical configuration of the system. Slow varying non-common path errors after the coronagraph also degrade the calibration procedure and require frequent update of the dictionary. With the goal of calibrating PSF on the fly during on-sky observations, we emphasize on calculating the effect of individual low-order modes on the science image in the dictionary.

3.1 Aberration model

In our simulation, we have considered a VVC at the focal plane in Fig. 1. Using LLOWFS, the starlight diffracted outside of the geometrical pupil in the Lyot plane is reflected by the RLS towards a reimaging focal plane. To build a library of response of the residuals on the starlight leakage, we applied known tip-tilt errors at the entrance pupil in Fig. 1 and precomputed the synchronized LLOWFS measurements and their corresponding science equivalents. We generated a matrix of aberrations A such that the size of A is m^n, where m is the number of images and n is the number of modes. For our simulation, we have considered only tip and tilt modes i.e. $n = 2$. The matrix A is represented as

$$A = \begin{bmatrix} \Phi_{11} & \dots & \Phi_{1m} \\ \vdots & \Phi_{xy} & \vdots \\ \Phi_{m1} & \dots & \Phi_{mn} \end{bmatrix} .$$

The rows and columns of matrix A simulates tip and tilt errors such that

$$\Phi_{xy} = Z_1\alpha_x + Z_2\alpha_y \ , \tag{12}$$

where Z_1 and Z_2 are the Zernike phasemap for modes tip and tilt with an amplitude α_x and α_y respectively. The aberration model (dictionary) is built by applying amplitudes (α_x, α_y) within $\pm$ 0.12 λ/D with a step size of 0.001 λ/D, therefore containing $m = 240$ images per row and a total of 240^n images for 2 modes. For each Φ_{xy} applied at the entrance pupil of Fig. 1, the LLOWFS ($DI_{R_{xy}}$) and science camera images ($DI_{S_{xy}}$) are recorded simultaneously. An example of such an aberration model is shown in Fig. 3.

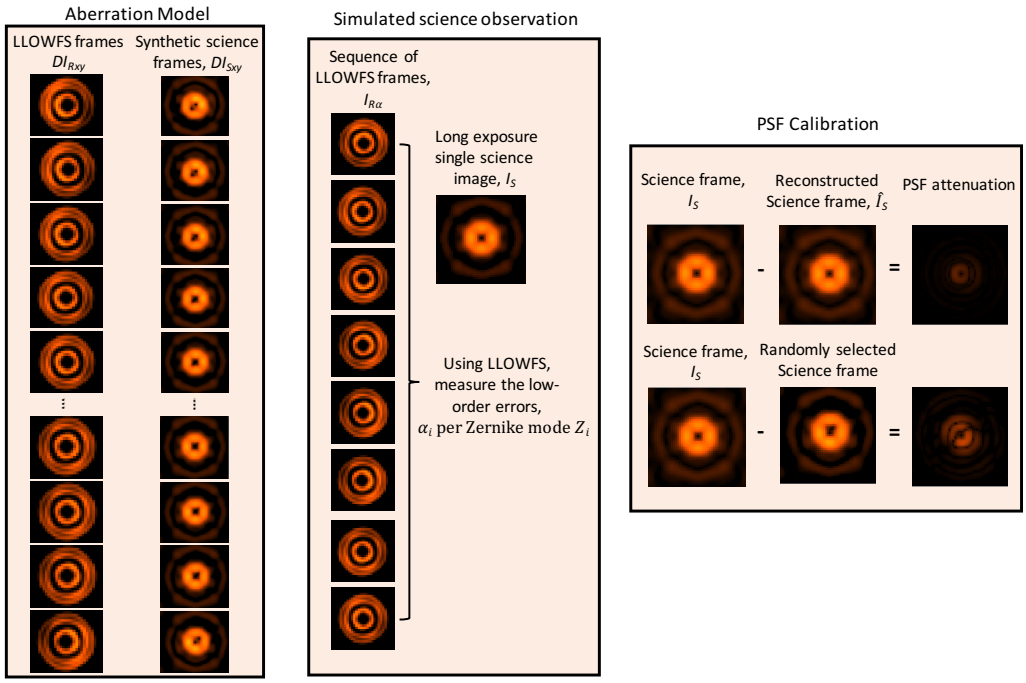

Figure 3. Procedure for using LLOWFS telemetry to calibrate the coronagraphic PSF (simulated case with a vector vortex coronagraph). An aberration model can be build by applying tip-tilt errors within $\pm$ 0.12 λ/D with a step size of 0.001 λ/D and synchronously saving the LLOWFS and the science camera images. During science observation, the science image can be reconstructed by selecting the best matched synthetic images from the aberration model (refer § 3). The reconstructed image obtained using proposed post-processing method when subtracted from the long exposure science image can significantly calibrate uncorrected pointing residuals.

3.2 Simulating science observation

To simulate a typical coronagraphic science observation, we generated a cube of 200 phasemaps with random tip-tilt errors with amount of amplitude ($\boldsymbol{\alpha}$) constrained within the linear range of LLOWFS. Sequences of short exposure LLOWFS frames ($I_{R_{\boldsymbol{\alpha}}}$) and science frames ($I_{S_{\boldsymbol{\alpha}}}$) are acquired. To simulate a long exposure science image (I_S), we averaged the 200 short exposure science frames ($I_{S_{\boldsymbol{\alpha}}}$). Then using LLOWFS equation 10, the tip-tilt errors α_i are estimated per Zernike mode Z_i (for tip mode, $i = 1$ and tilt mode, $i = 2$) per LLOWFS frames ($I_{R_{\boldsymbol{\alpha}}}$).

3.3 Predicting long exposure science image

Now the next step involves selecting a batch of synthetic science images ($\hat{I}_{S_{xy}}$) from the aberration model ($DI_{S_{xy}}$) that best represent the residuals leaked in the long exposure science image (I_S). In order to select the best match of synthetic images from the dictionary, we directly compared the applied tip-tilt amplitude (α_x, α_y) in the dictionary with the estimated (α_1, α_2) tip-tilt amplitude in the short exposure LLOWFS images ($I_{R_{\boldsymbol{\alpha}}}$).

The corresponding synthetic science images ($\hat{I}_{S_{xy}}$) are selected from $DI_{S_{xy}}$ for which $\sqrt{<(\alpha_x - \alpha_1)^2>}$ and $\sqrt{<(\alpha_y - \alpha_2)^2>}$ was minimum. These selected synthetic images are then averaged to built a single reconstructed science image ($\hat{I}_S$) that best represent the long exposure science PSF (I_S). To calibrate the pointing

residual, $\hat{I}_S$ is simply subtracted from I_S as shown in the PSF calibration box in Fig. 3. The attenuation in the tip-tilt residuals is quite prominent. To mimic a standard PSF subtraction calibration, we also select a set of random synthetic science frames from the dictionary to subtract their average from I_S and show that significant amount of errors are left uncalibrated in the final subtracted image. Note that all images are at same brightness scale.

In order to improve the reconstruction process, instead of simply averaging synthetic science images ($\hat{I}_{S_{xy}}$), we considered $\hat{I}_{S_{xy}}$ as a set of reference images and computed a synthetic PSF using the PCA-based KLIP algorithm, by projecting the long exposure science image (I_S) on the 20 first principal components of this library. Since this set of references was selected from actual LLOWFS measurement during the long exposure acquisition, it is well representative of the various PSF states that compose the final science image. Moreover, compared to the averaged-reference calibration, the KLIP calibration is customized to the long exposure science image, which makes it more robust to NCPE or poorly sampled pre-acquired dictionary.

The standard deviation of different image profiles as a function of angular separation is presented in Fig. 4. The standard deviation over the pixels is calculated within an annulus of diameter 1 λ/D. Three simulated profiles of PSF subtraction are described as follows: Solid blue line represents the subtraction using the best fit cleaned science image ($\hat{I}_S$) computed via the proposed post-processing procedure; solid red line represents the subtraction using a random match cleaned science image and solid green line is the subtraction obtained with a cleaned image computed by performing PCA on the best matched synthetic science images ($\hat{I}_{S_{xy}}$). Although no detector noise has been taken into account in our simulation, reconstruction using the PCA appears to be cleaner than simply averaging the best matched synthetic science images to calibrate the pointing residuals.

To study the effect of NCPA and the robustness of our calibration method, static tip-tilt errors are also induced in the science beam (unseen by the LLOWFS) after the RLS in Fig. 1. The PSF subtraction profiles using the average of $\hat{I}_{S_{xy}}$ via proposed calibration approach and the PCA on $\hat{I}_{S_{xy}}$ are respectively shown in dashed blue and green line in Fig. 4. No significant degradation is noticed in the reconstruction of the respective method as compared with simulation done without considering NCPA. This is expected because the information related to most of the NCP errors are already computed in the dictionary. However, when NCPA of first five Zernike modes (tip, tilt, focus, oblique and right astigmatisms) are added downstream of the RLS, the performance of reconstruction using the PCA has been degraded significantly as shown in dot dashed green line in Fig. 4. This is because there is no pre-calibrated information regarding focus, oblique and right astigmatism aberrations in the dictionary so the PCA could not represent the structure contributed by these aberrations. The performance of reconstruction via proposed calibration approach (average of $\hat{I}_{S_{xy}}$) under NCPA (dot dashed blue line) is almost similar to random match method with no NCPA error (solid red line).

Nevertheless, reconstructing long exposure science image ($\hat{I}_S$) from a set of synthetic images ($\hat{I}_{S_{xy}}$) using the PCA is still one and two orders of magnitude better than the best and random match methods under the NCPA of 5 Zernike modes respectively. This demonstrates that calibration of $\hat{I}_{S_{xy}}$ using PCA is quite robust to NCPA. We expect the performance to improve after pre-computing the effect of other Zernike modes in the dictionary.

4. CONCLUSION

We present a preliminary effort on calibrating the starlight leak in post-processing of the coronagraphic images using the LLOWFS telemetry i.e. by reconstructing the science image from a set of best matched synthetic images selecetd from a pre-computed dictionary. The dictionary is obtained by applying known tip-tilt errors in the coronagraphic system unlike in Ref. 9. Pre-computing the contribution of all the possible low-order aberrations on the coronagraphic leak can not only reduce the requirement of frequently updating the dictionary as required in Ref. 9 approach but can also address NCPA not seen by the LLOWFS. In this proceeding, we have presented simulation (without considering any noise) of calibrating the PSF using tip-tilt telemetry from the LLOWFS for a vector vortex coronagraph.

Our approach is currently rudimentary and we are investigating two major problems: (1) how to create a compact dictionary that contain a wide range of low-order wavefront aberration information and (2) computing an empirical model to precisely select the best synthetic images from the dictionary using interpolation methods. A precise reconstruction model can also derive the requirement on the size of the dictionary for example if a

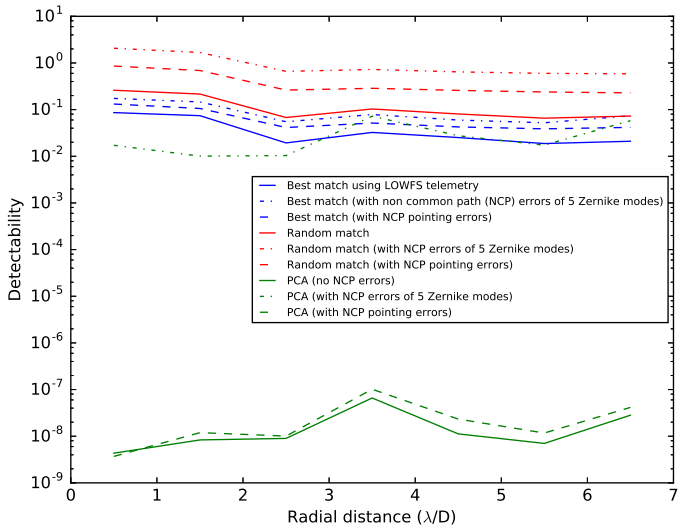

Figure 4. Different PSF subtraction profiles as a function of angular separation are presented. Each profile is the standard deviation of the pixels in an annulus of diameter 1 λ/D. Science image reconstruction ($\hat{I}_S$) from synthetic images $\hat{I}_{S_{xy}}$ using the PCA is much more cleaner than simply averaging $\hat{I}_{S_{xy}}$. *Note: Synthetic/Reference images are selected from the dictionary, which is generated using the LLOWFS telemetry.*

coarse dictionary with limited number of amplitude per aberration would be sufficient or indeed a fine dictionary with large range of amplitude is required. Inducing fake planets at different angular separation will be useful to determine the limiting contrast. Further such simulations defining a rigorous reconstruction model and addressing the problem of the dictionary size are intended for future publication.

5. ACKNOWLEDGEMENT

This research was supported by an appointment to the NASA Postdoctoral Program at the Jet Propulsion Laboratory, California Institute of Technology, administered by Universities Space Research Association under contract with NASA. The author gratefully acknowledge the support and help from Subaru Telescope and the Observatory staff. The research with the Lyot-based low-order wavefront sensor was conducted at the Subaru Telescope, which was partly supported by a Grant-in-Aid for Science Research in a Priority Area from MEXT, Japan. The author would like to thank Frédéric Vogt, Dimitri Mawet, James Kent Wallace and Matthew Kenworthy for meaningful and helpful discussions on PSF calibration using WFS telemetry method. We would also like to acknowledge the Hubble Fellowship grant #HF2-51355 awarded by the Space Telescope Science Institute, which is operated by the Association of Universities for Research in Astronomy, Inc., for NASA, under contract NAS5-26555.

REFERENCES

[1] Guyon, O., Pluzhnik, E. A., Kuchner, M. J., Collins, B., and Ridgway, S. T., "Theoretical Limits on Extrasolar Terrestrial Planet Detection with Coronagraphs," *Astrophys. J.* **167**, 81–99 (Nov. 2006).

[2] Guyon, O., "Limits of Adaptive Optics for High-Contrast Imaging," *Astrophys. J.* **629**, 592–614 (Aug. 2005).

[3] Mawet, D., Pueyo, L., Lawson, P., Mugnier, L., Traub, W., Boccaletti, A., Trauger, J. T., Gladysz, S., Serabyn, E., Milli, J., Belikov, R., Kasper, M., Baudoz, P., Macintosh, B., Marois, C., Oppenheimer, B., Barrett, H., Beuzit, J.-L., Devaney, N., Girard, J., Guyon, O., Krist, J., Mennesson, B., Mouillet, D., Murakami, N., Poyneer, L., Savransky, D., Vérinaud, C., and Wallace, J. K., "Review of small-angle coronagraphic techniques in the wake of ground-based second-generation adaptive optics systems," in [*Society of*

Photo-Optical Instrumentation Engineers (SPIE) Conference Series], *Society of Photo-Optical Instrumentation Engineers (SPIE) Conference Series* **8442**, 4 (Sept. 2012).

[4] Guyon, O., Matsuo, T., and Angel, R., "Coronagraphic Low-Order Wave-Front Sensor: Principle and Application to a Phase-Induced Amplitude Coronagraph," *Astrophys. J.* **693**, 75–84 (Mar. 2009).

[5] Singh, G., Martinache, F., Baudoz, P., Guyon, O., Matsuo, T., Jovanovic, N., and Clergeon, C., "Lyot-based Low Order Wavefront Sensor for Phase-mask Coronagraphs: Principle, Simulations and Laboratory Experiments," *Pub. Astron. Soc. Pacific* **126**, 586–594 (June 2014).

[6] Wallace, J. K., Rao, S., Jensen-Clem, R. M., and Serabyn, G., "Phase-shifting Zernike interferometer wavefront sensor," in [*Optical Manufacturing and Testing IX*], *Proceedings of the SPIE* **8126**, 81260F (Sept. 2011).

[7] Marois, C., Lafrenière, D., Doyon, R., Macintosh, B., and Nadeau, D., "Angular Differential Imaging: A Powerful High-Contrast Imaging Technique," *Astrophys. J.* **641**, 556–564 (Apr. 2006).

[8] Martinache, F., Guyon, O., Jovanovic, N., Clergeon, C., Singh, G., Kudo, T., Currie, T., Thalmann, C., McElwain, M., and Tamura, M., "On-Sky Speckle Nulling Demonstration at Small Angular Separation with SCExAO," *Pub. Astron. Soc. Pacific* **126**, 565–572 (June 2014).

[9] Vogt, F. P. A., Martinache, F., Guyon, O., Yoshikawa, T., Yokochi, K., Garrel, V., and Matsuo, T., "Coronagraphic Low-Order Wavefront Sensor: Postprocessing Sensitivity Enhancer for High-Performance Coronagraphs," *Pub. Astron. Soc. Pacific* **123**, 1434–1441 (Dec. 2011).

[10] Singh, G., Lozi, J., Guyon, O., Baudoz, P., Jovanovic, N., Martinache, F., Kudo, T., Serabyn, E., and Kuhn, J., "On-Sky Demonstration of Low-Order Wavefront Sensing and Control with Focal Plane Phase Mask Coronagraphs," *Pub. Astron. Soc. Pacific* **127**, 857–869 (Oct. 2015).

[11] Singh, G., "Thesis: Low-order wavefront control and calibration for phase mask coronagraphs. Instrumentation and Methods for Astrophysics $< tel - 01221421 >$," *Observatoire de Paris* (2015).

[12] Jovanovic, N., Martinache, F., Guyon, O., Clergeon, C., Singh, G., Kudo, T., Garrel, V., Newman, K., Doughty, D., Lozi, J., Males, J., Minowa, Y., Hayano, Y., Takato, N., Morino, J., Kuhn, J., Serabyn, E., Norris, B., Tuthill, P., Schworer, G., Stewart, P., Close, L., Huby, E., Perrin, G., Lacour, S., Gauchet, L., Vievard, S., Murakami, N., Oshiyama, F., Baba, N., Matsuo, T., Nishikawa, J., Tamura, M., Lai, O., Marchis, F., Duchene, G., Kotani, T., and Woillez, J., "The Subaru Coronagraphic Extreme Adaptive Optics System: Enabling High-Contrast Imaging on Solar-System Scales," *Pub. Astron. Soc. Pacific* **127**, 890–910 (Oct. 2015).

[13] Soummer, R., Pueyo, L., and Larkin, J., "Detection and Characterization of Exoplanets and Disks Using Projections on Karhunen-Loève Eigenimages," *Astrophys. J. Lett.* **755**, L28 (Aug. 2012).

[14] Clergeon, C., Guyon, O., Martinache, F., Veran, J.-P., Gendron, E., Rousset, G., Correia, C., and Garrel, V., "The Subaru Coronagraphic Extreme AO High Speed and High Sensitivity Wavefront Sensors," in [*Proceedings of the Third AO4ELT Conference*], Esposito, S. and Fini, L., eds., 95 (Dec. 2013).

[15] Guyon, O., Hayano, Y., Tamura, M., Kudo, T., Oya, S., Minowa, Y., Lai, O., Jovanovic, N., Takato, N., Kasdin, J., Groff, T., Hayashi, M., Arimoto, N., Takami, H., Bradley, C., Sugai, H., Perrin, G., Tuthill, P., and Mazin, B., "Adaptive optics at the Subaru telescope: current capabilities and development," in [*Society of Photo-Optical Instrumentation Engineers (SPIE) Conference Series*], *Society of Photo-Optical Instrumentation Engineers (SPIE) Conference Series* **9148**, 1 (Aug. 2014).